Chemical Science

EDGE ARTICLE

View Article Online
View Journal

Cite this: DOI: 10.1039/d6sc01335j

All publication charges for this article have been paid for by the Royal Society of Chemistry

Precise construction of symmetrically coordinated triatomic zirconium catalyst for efficient oxygen reduction

Anaer Husile, Tianmi Tang, Liyuan Xiao, Xue Bai, Zhenlu Wang * and Jingqi Guan *

Received 14th February 2026
Accepted 21st April 2026

DOI: 10.1039/d6sc01335j

rsc.li/chemical-science

Developing an environmentally friendly, highly efficient, and stable electrocatalyst for the oxygen reduction reaction (ORR) holds critical importance for advancing the commercial viability of zinc–air batteries (ZABs). The d-band electronic structure of metal atoms in triatomic catalysts (TACs) can be precisely regulated to achieve the optimal adsorption energy for oxygen intermediates (*OOH, *O and *OH). Here, a TAC Zr_3/NG with $Zr_3O_1N_6$ active sites has been successfully synthesized by a Joule heating method for the ORR. The Zr_3/NG demonstrates a half-wave potential ($E_{1/2}$) of 0.857 V, better than that of single-atom Zr_1/NG and commercial Pt/C. Furthermore, the ZAB based on Zr_3/NG can achieve a maximum peak power density of 164.3 mW cm^{-2} and retains stable operation for over 175 h. Theoretical studies reveal that the $Zr_3O_1N_6$ coordination configuration shifts the d-band center of zirconium toward the Fermi level, effectively adjusting the adsorption energy of the oxygen intermediate by elongating the O–O bond through bridge adsorption, thereby effectively promoting the breaking of the bond. This study reveals the synergistic effect of triatomic zirconium active centers for improving the ORR performance.

Introduction

With the decreasing availability of non-renewable fuel energy and the aggravation of environmental problems, the development of green and environmentally friendly energy technology has become a top priority of scientific research.[1–3] Among various energy storage systems, rechargeable ZABs stand out as an attractive emerging technology, owing to their notable attributes including high energy density, operational safety, cost-effectiveness, versatile applicability, and environmental sustainability.[4,5] However, ZABs are susceptible to the ORR during discharging. The slow kinetics of the ORR process requires a complex catalyst system to accelerate the reaction. Studies have shown that noble metal-based catalysts such as Pt have strong catalytic activity for the ORR process, but their crustal abundance and cost-effectiveness hinder further industrialization.[6,7] Therefore, it is urgent to develop green, environmentally friendly and cheap high-performance ORR catalysts. Over the last ten years, significant research efforts have been directed toward developing catalysts free of precious metals, including heteroatom-doped carbon materials, metallic alloys, transition-metal-based compounds, and hybrid composites.[8–10] However, simultaneously achieving high ORR activity and outstanding durability is still a challenge for current research.

Institute of Physical Chemistry, National Demonstration Center for Experimental Chemistry Education, College of Chemistry, Jilin University, 2519 Jiefang Road, Changchun 130021, China. E-mail: wzl@jlu.edu.cn; guanjq@jlu.edu.cn

Single-atom catalysts have shown great potential in the field of energy storage due to their high metal utilization, uniform active centers, high selectivity and adjustable electronic structure. For single-atom Zr catalysts, Zr atoms contribute to the adsorption and reduction of oxygen molecules, promote the formation of oxygen vacancies, and accelerate the oxygen reduction process.[11] In addition, Zr metal itself has excellent corrosion resistance, which enables it to maintain long-term stable catalysis in harsh environments. At the same time, the doping of N atoms can change the electronic structure of the carbon support surface, enhance the adsorption of oxygen intermediates, reduce the reaction barrier, and improve the ORR reactivity.[12,13] However, the loading of single-atom catalysts is usually low, resulting in limited current density, which makes it difficult to meet the needs of large-scale applications. In addition, the structure of single-atom metal catalysts is unstable, and they agglomerate very easily during high-temperature calcination, which prevents them from achieving the predicted effect.[14]

To overcome these limitations, the research focus has gradually shifted toward diatomic catalysts (DACs) and even polyatomic catalysts.[15,16] By constructing adjacent metal sites and leveraging the electronic and geometric synergy between them, the adsorption behavior of reaction intermediates can be further optimized, thereby overcoming the activity limitations of single-atom sites. Among these, triatomic catalysts represent an emerging frontier. Through the careful design of the coordination microenvironment in trinuclear metal clusters, it is possible to achieve more precise control over multi-step reaction pathways, leading to overall performance that surpasses that of both diatomic and single-atom catalysts. However, current research on TACs, especially well-defined triatomic systems based on non-traditional active metals such as zirconium, remains in the exploratory stage. The structure–performance relationship and the upper limit of their performance are still not well understood.

In light of this, this paper proposes a novel design strategy for constructing triatomic catalysts. Utilizing the Joule-heating method, we precisely anchored $Zr_3O_1N_6$ active sites onto a nitrogen-doped graphene support, successfully synthesizing the Zr_3/NG TAC. Zr_3/NG demonstrates outstanding activity, stability, and poisoning resistance for the ORR process, surpassing commercial Pt/C catalysts. DFT studies reveal that the $Zr_3O_1N_6$ moiety serves as the active center for the ORR. The triatomic configuration modulates the d-band center of the catalyst and exhibits a high density of states, effectively enhancing the oxygen reduction activity. Furthermore, the ZAB assembled with Zr_3/NG delivers an open-circuit voltage of 1.463 V and retains excellent cycling stability for up to 175 h. The $Zr_3O_1N_6$ structure is expected to optimize the ORR pathway through the synergistic effect of the trinuclear zirconium cluster and the electronic modulation of the bridging oxygen atoms. This work not only proposes a novel strategy for designing efficient and stable zirconium-based multiatomic catalysts, but also offers a promising cathode material for advancing the practical deployment of energy systems such as ZABs.

Results and discussion

Synthesis and characterization

As shown in Fig. 1a, the tri-atomic Zr_3 catalyst was constructed by a rapid Joule heating technique. Specifically, a Zr-based complex with Zr_3 cluster bridged by one oxygen atom and each Zr atom coordinated with five oxygen atoms and one cyclopentadienyl (Cp) group to form a trigonal structure was first prepared (Fig. S1). ^{1}H nuclear magnetic resonance (NMR) spectroscopy reveals detailed structural information, confirming the successful synthesis of the Zr_3 precursor (Fig. S2).[17] After that, the Zr_3 precursor was attached to graphene oxide (GO) by an ultrasonically assisted method, and Zr_3/GO was obtained by rotary evaporation. Finally, Zr_3/GO was rapidly annealed in an NH_3 atmosphere within 3 s in a Joule heating device to obtain Zr_3/NG. For comparison, Zr_1/NG was also prepared by a similar method. The transmission electron microscopy (TEM) images of Zr_3/NG are shown in Fig. 1b and c. Zr_3/NG exhibits a lamellar structure and there is no obvious accumulation of metal-based nanoparticles. The energy dispersive spectroscopy (EDS) mapping of Zr_3/NG shows that Zr, N, O and C are uniformly distributed on the NG substrate (Fig. 1d and e). The distribution and configuration of Zr atoms in Zr_3/NG are identified by aberration-corrected high-angle annular dark-field scanning transmission electron microscopy (AC-HAADF-STEM). As shown in Fig. 1f and g, there are triangular bright spots on the nitrogen-doped graphene substrate, and the atomic spacing is *ca.* 0.243 nm, 0.275 nm and 0.346 nm in a typical tri-atomic site (Fig. 1h and i), which is consistent with the results of atomic intensity distribution analysis (Fig. 1j), indicating triangular triatomic zirconium configuration.

The crystal structures of NG, Zr_1/NG and Zr_3/NG were analysed by X-ray diffraction (XRD). As shown in Fig. 2a, except for two obvious peaks due to graphite, there are no other obvious peaks due to Zr-based nanoparticles, indicating that Zr is well distributed on the surface of NG.[18] The oxidation state of Zr in Zr_3/NG was investigated using X-ray photoelectron spectroscopy (XPS). The XPS full spectrum shows that Zr_3/NG contains C, O, N, and Zr elements (Fig. S3). As shown in Fig. 2b, the high-resolution Zr 3d spectrum exhibits two orbital peaks at 184.52 eV (Zr $3d_{3/2}$) and 182.2 eV (Zr $3d_{5/2}$), indicating that the oxidation state of Zr is +4.[19] Simultaneously, the broadening of the Zr 3d peak shape suggests that Zr is in a complex coordination environment. The high-resolution N 1s spectrum of Zr_3/NG after convolution shows five characteristic peaks, which are attributed to Zr–N (397.3 eV), pyrrolic N (400.1 eV), pyridinic N (398.5 eV), graphitized N (401.2 eV) and oxidized N (404.1 eV), indicating the successful coordination of the Zr–N bond (Fig. 2c).[20–22] The formation of pyridinic nitrogen and graphitized nitrogen is helpful for improving the ORR performance and electron transfer rate, respectively.[23]

Further studies on the oxidation state and coordination structure of the metal active sites were conducted using X-ray absorption spectroscopy (XAS).[24] The Zr K-edge X-ray absorption near-edge structure (XANES) spectra of Zr foil, ZrO_2, Zr_1/NG, and Zr_3/NG are shown in Fig. 2d. The absorption edge spectra of Zr_3/NG and Zr_1/NG are very close to that of ZrO_2, indicating that the oxidation state of Zr in both Zr_3/NG and Zr_1/NG is +4, which is consistent with the XPS analysis results. The local coordination environment of Zr in the different catalysts was investigated using Fourier-transform extended X-ray absorption fine structure (FT-EXAFS) spectroscopy (Fig. 2e). The FT-EXAFS curves of both the Zr_1/NG and Zr_3/NG samples show a distinct peak at ∼1.7 Å, which can be attributed to Zr–N/O coordination.[25] The peak at ∼3.03 Å in the FT-EXAFS spectra of Zr_3/NG corresponds to the Zr–O–Zr scattering path observed in ZrO_2 and differs from the Zr–Zr scattering path in Zr foil.[26] Here, the coordination numbers for Zr–N and Zr–O are approximately 1.9 and 1.1, respectively, with corresponding bond lengths of about 1.82 Å and 1.93 Å. Furthermore, the Zr–Zr distance in the Zr–O–Zr path is ∼3.16 Å, and the coordination number is ∼1 (Fig. 2f, S4c and Table S1). The fitting results for Zr_1/NG indicate that its coordination environment corresponds to ZrN_4 (Fig. S4a, b, and Table S1). Additionally, the arrangement of backscattering atoms was analysed using Zr K-edge wavelet transform (WT-EXAFS) spectroscopy to further explore the coordination structure of Zr_3/NG. The WT contour plots of Zr_3/NG, Zr_1/NG, and the reference samples are shown in Fig. 2h, i, and S5. Among these, the strongest peak for Zr_3/NG appears at ∼5.1 $Å^{-1}$, consistent with Zr–O/N coordination, while a relatively strong peak at ∼9.5 $Å^{-1}$ corresponds to Zr–O–Zr backscattering. Notably, no Zr–Zr metal coordination signal was detected in Zr_3/NG. Based on the above analysis, it can be inferred that the coordination structure of Zr_3/NG consists of an oxygen-bridged, nitrogen-terminated trinuclear Zr cluster, namely $Zr_3O_1N_6$ configuration (Fig. 2g).

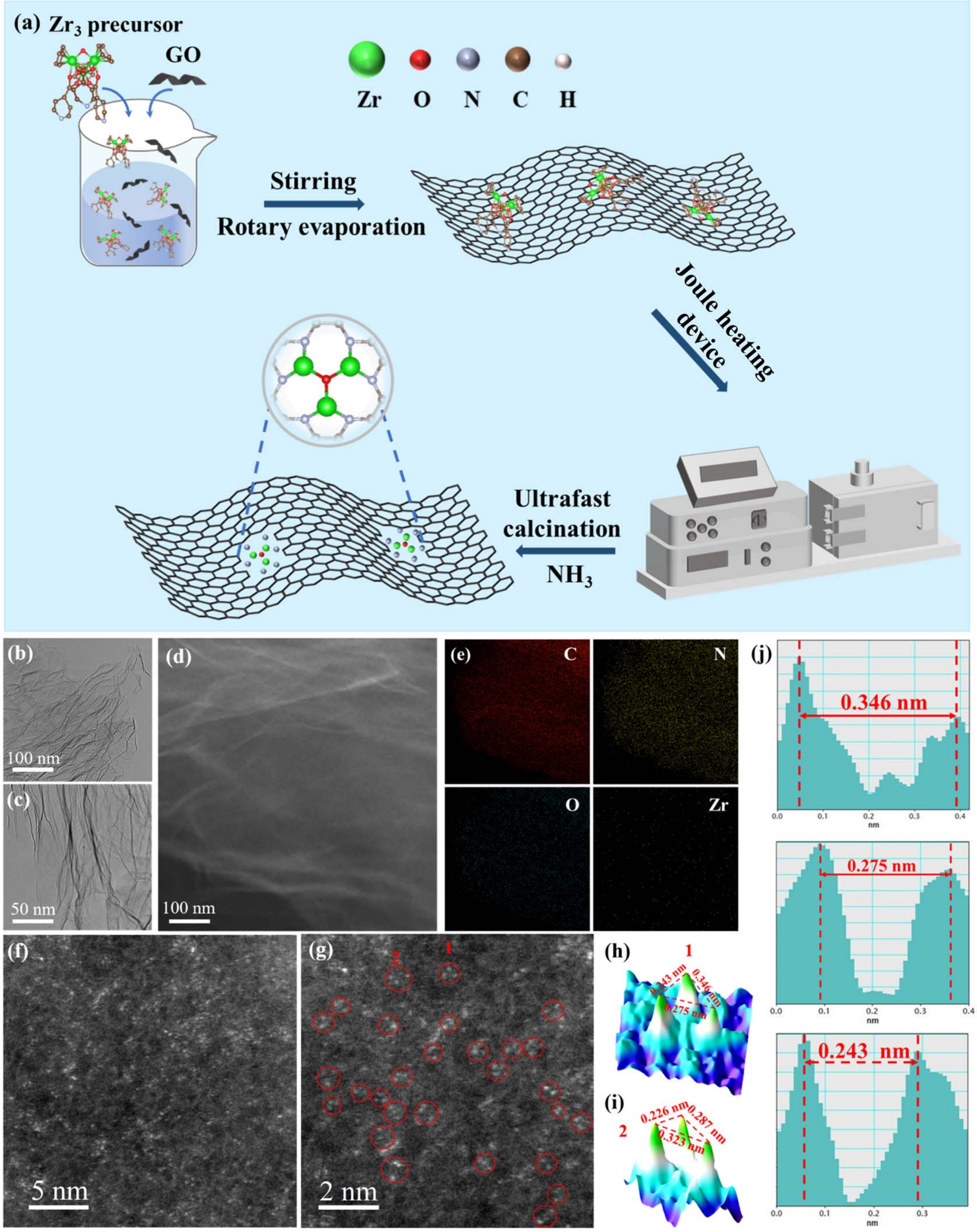

Fig. 1 (a) The synthesis route of Zr_3/NG. (b and c) HRTEM images. (d) HRTEM and (e) EDS elemental mapping of C, N, O and Zr. (f and g) HAADF-STEM images of Zr_3/NG. (h–j) Schematic diagram of different atomic spacing.

ORR performance. To examine the influence of the trigonal pyramidal structure on the catalytic performance for alkaline ORR (0.1 M KOH solution), we compared the Zr_3/NG catalyst with Zr_1/NG, commercial Pt/C, and NG samples using cyclic voltammetry (CV) and linear sweep voltammetry (LSV). The CV curve of Zr_3/NG exhibits a more positive oxygen reduction peak, indicating its higher ORR activity (Fig. S6). Compared with Zr_1/NG and metal-free NG, Zr_3/NG shows significantly enhanced ORR activity, with a half-wave potential reaching 0.857 V, surpassing that of commercial Pt/C ($E_{1/2} = 0.827$ V), the reference samples Zr_1/NG ($E_{1/2} = 0.837$ V) and NG ($E_{1/2} = 0.811$ V), and many advanced catalysts reported previously (Fig. 3a and Table S2). This can be attributed to the synergistic effect among the trinuclear zirconium atoms and the electronic modulation by the bridging oxygen atom. Furthermore, Zr_3/NG delivers a higher limiting current density (5.1 mA cm^{-2}) and a lower Tafel slope (48.2 mV dec^{-1}) than Pt/C (4.4 mA cm^{-2} and 76.6 mV dec^{-1}), Zr_1/NG (2.7 mA cm^{-2} and 58.7 mV dec^{-1}), and NG (1.9

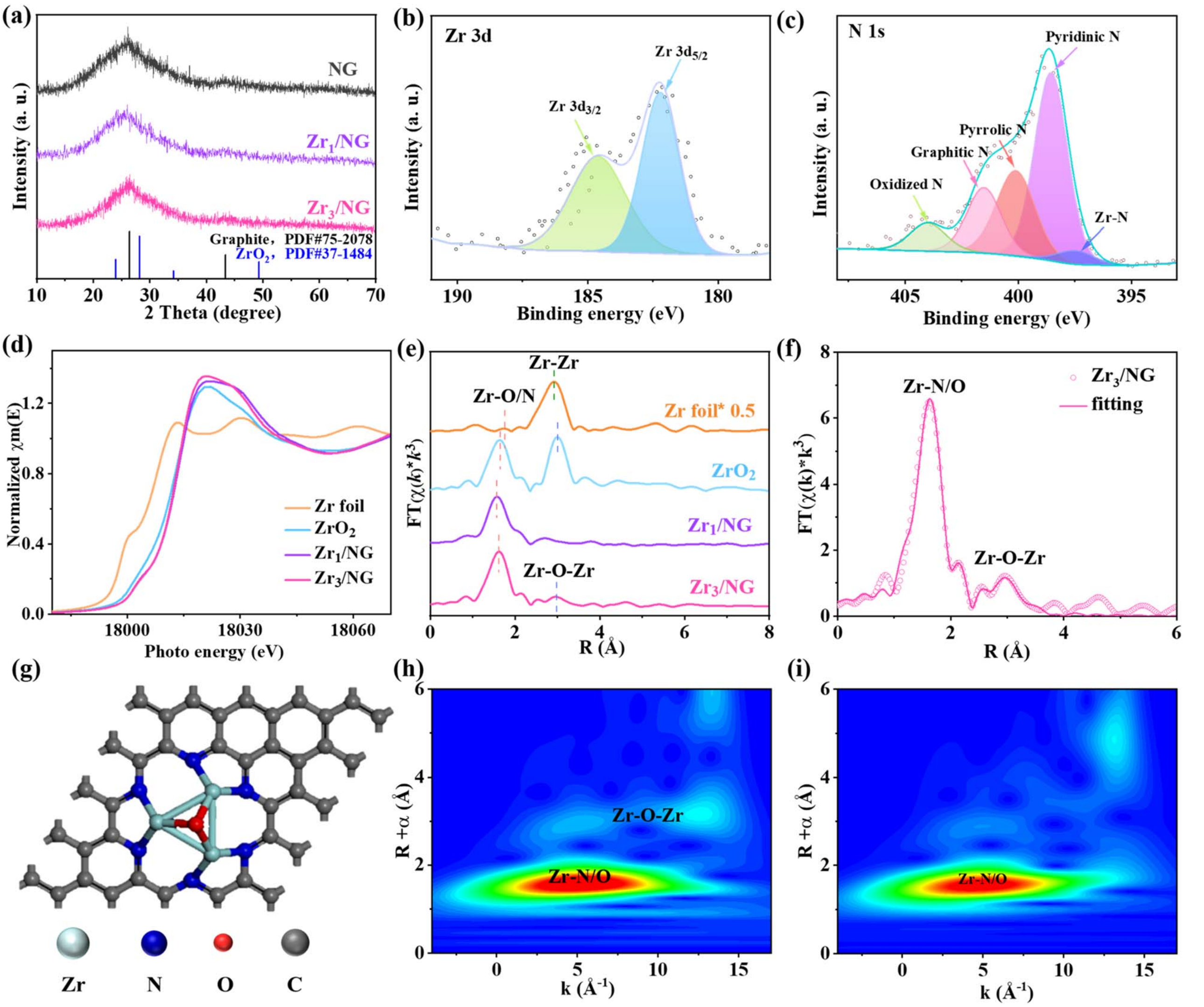

Fig. 2 (a) XRD patterns. XPS spectra of (b) Zr 3d and (c) N 1s. (d) Zr K-edge XANES spectra of Zr_3/NG, Zr_1/NG, ZrO_2 and Zr foil. (e) FT-EXAFS spectra. (f) FT-EXAFS of the R-space fitting spectra for Zr_3/NG. (g) The model of triatomic $Zr_3O_1N_6$. WT-EXAFS plots of (h) Zr_3/NG and (i) Zr_1/NG.

mA cm^{-2} and 61.4 mV dec^{-1}), confirming its superior ORR kinetics and significantly enhanced intrinsic activity (Fig. 3b).[27] We further studied the influence of metal loading (Fig. S7) and annealing temperature (Fig. S8) on the catalytic activity. Experimental results show that the 1.2 wt%-Zr_3/NG sample annealed at 1400 °C exhibits the highest ORR activity. By fitting LSV curves at different rotation rates, the ORR electron-transfer kinetics of Zr_3/NG and Pt/C were explored.[28] In the potential range of 0.4–0.6 V, the average electron-transfer number for Zr_3/NG is 3.89 (Fig. 3c). In addition, we employed a RRDE to study the reaction selectivity of the ORR process. At an applied potential of 0.6 V, the H_2O_2 yield of Zr_3/NG is less than 10%, and the electron-transfer number is around 3.9 (Fig. 3d), indicating its strong capability for O–O bond cleavage. Double-layer capacitance (C_{dl}) and the electrochemical active surface area (ECSA) are important indicators for evaluating electrocatalytic materials.[29] These values were obtained from CV curves at different scan rates. The C_{dl} and ECSA of Zr_3/NG are 17.58 mF cm^{-2} and 455.8 cm^2, respectively, which are higher than those of Zr_1/NG, Pt/C and NG, suggesting that Zr_3/NG possesses more active sites and thus exhibits higher activity during electrocatalysis (Fig. 3e and S9–S12). Long-term stability and poisoning tolerance are key metrics for assessing catalyst performance.[30] During the 17 h durability test, Zr_3/NG retains 90.3% of its initial current density, whereas Pt/C retains only 71.3% (Fig. 3f). Moreover, Zr_3/NG shows excellent poisoning resistance. When 1 mL of CH_3OH is injected into the O_2-saturated KOH electrolyte, the current density change of Zr_3/NG is almost negligible, while that of commercial Pt/C drops rapidly due to methanol oxidation side reactions and only recovers to about 50% afterward (Fig. 3g). In summary, the trigonal-pyramidal-structured Zr_3/NG can effectively and stably promote the alkaline ORR process.

To further investigate the reaction mechanism of the ORR process, we employed *in situ* electrochemical Raman spectroscopy to monitor the catalytic process in real time. As shown in

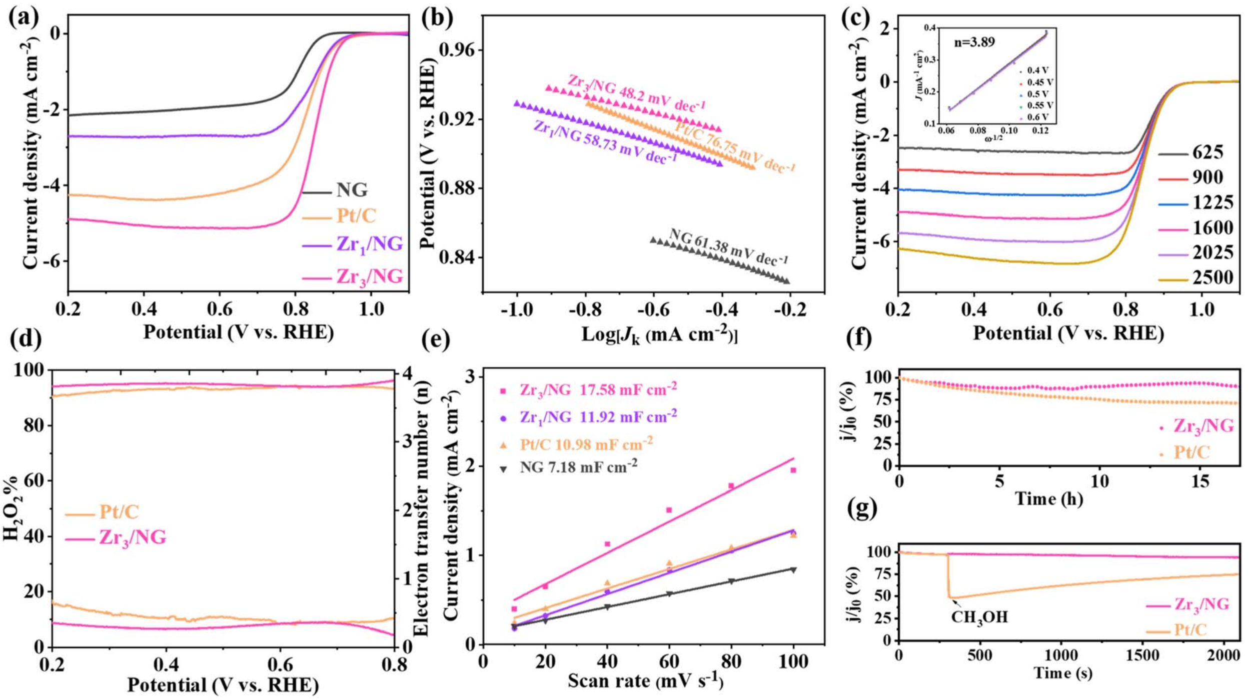

Fig. 3 (a) LSV curves in oxygen-saturated 0.1 M KOH. (b) Tafel slope of Zr_3/NG, Zr_1/NG, Pt/C and NG. (c) LSV curves of Zr_3/NG at different rotation speeds (the inset: K-L plots). (d) H_2O_2 yield and electron transfer number on Zr_3/NG and Pt/C. (e) Electric double layer capacitance of Zr_3/NG, Zr_1/NG, Pt/C and NG at different scan rates. (f) Chronoamperometric current (i–t) curves of Zr_3/NG and Pt/C. (g) The anti-methanol interference ability curves of Zr_3/NG and Pt/C.

Fig. S13, at different applied potentials, the Raman spectra of Zr_3/NG exhibit characteristic peaks at 1350 cm^{-1} and 1590 cm^{-1}, which are attributed to the D-band and G-band (in O_2-saturated 0.1 M KOH solution). At applied potentials between 0.2 and 1.2 V, a new Raman signal appears at 1553 cm^{-1}, which was assigned to the stretching vibration of the OOH* intermediate.[31–33] The above results further confirm that OOH* is a key intermediate in the ORR process.

Study of the ORR mechanism. To further investigate the ORR mechanism on Zr_3/NG, density functional theory (DFT) calculations were performed. Firstly, by combining the XAFS and AC-HAADF-STEM results, we constructed and optimized a $Zr_3O_1N_6$ model (Fig. S14a). For comparison, a ZrN_4 model was also built for Zr_1/NG (Fig. S14b). Fig. 4a and S15 display the adsorption configurations of OOH*, O*, and OH* intermediates on Zr_3/NG and Zr_1/NG. On the ZrN_4 active site, the intermediates adsorb in a *cis*-configuration, whereas on the $Zr_3O_1N_6$ site, O* and OH* adopt a bridging adsorption mode. Specifically, OOH* forms a bond with the central Zr atom, while the oxygen atoms of OH* and O* together with the metal atoms form a peroxo-bridge structure. This configuration favours the further adsorption and dissociation of O* and OH*, ultimately promoting the oxygen reduction process. Fig. 4b shows the Gibbs free energy changes for Zr_3/NG and Zr_1/NG upon adsorption of different reaction intermediates (OOH*, O*, and OH*). Among these steps, OH* → H_2O is identified as the rate-determining step (RDS) of the ORR. At $U = 0$ V, the free energies of the OH* → H_2O step for Zr_3/NG and Zr_1/NG are −1.83 eV and −2.88 eV, respectively. Fig. 4c and S16 present the differential charge density of the two models. Due to the electronegativity difference between Zr and N/O, charge rearrangement occurs in the $Zr_3O_1N_6$ geometry. In addition, the density of states (DOS) and partial density of states (PDOS) of Zr_3/NG and Zr_1/NG were also calculated. The d-band center of Zr_3/NG is at −0.775 eV, which is lower than that of Zr_1/NG (−0.652 eV), indicating a leftward shift of the d-band center for Zr_3/NG. According to the d-band center theory, a leftward shift of the d-band center relative to the Fermi level typically leads to an increased occupation of the antibonding states between the adsorbate and the metal surface, thereby weakening the interaction between the metal site and the adsorbed intermediates and lowering the reaction energy barrier. In contrast, during the reaction process, Zr_1/NG exhibits excessively strong adsorption of reaction intermediates, resulting in poisoning of the active sites and difficulty in product desorption, which limits the reaction rate. The above data indicate that the leftward shift of the d-band center in Zr_3/NG suppresses excessive adsorption of oxygen-containing intermediates at the $Zr_3O_1N_6$ sites (Fig. 4d and e), thereby reducing the reaction adsorption energy. In summary, the trigonal pyramidal $Zr_3O_1N_6$ structure possesses more accessible electronic states, enabling appropriate interactions with reaction intermediates and thus facilitating the overall ORR process.

Application of Zr_3/NG in ZABs. Benefiting from the excellent ORR performance of Zr_3/NG, we constructed it as the air cathode in a ZAB with a polished zinc plate as the anode for

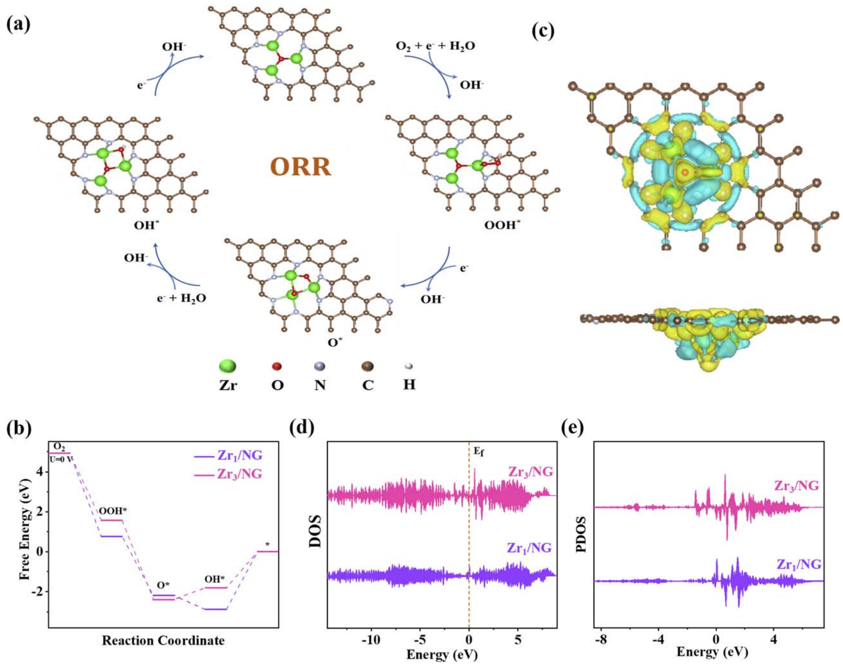

Fig. 4 (a) Illustration of the adsorption mode of ORR intermediates on Zr_3/NG. (b) Gibbs free energy diagram of Zr_3/NG at $U = 0$ V. (c) Charge density difference of Zr_3/NG. (d) DOS and (e) PDOS diagrams of Zr 3d orbitals in Zr_3/NG and Zr_1/NG.

application evaluation (Fig. 5a). The Zr_3/NG-based ZAB exhibits an open-circuit voltage (OCV) of 1.46 V and a maximum peak power density of 164.3 mW cm^{-2}, as confirmed by OCV measurements (Fig. 5b) and polarization curves (Fig. 5c). Both values surpass those of the Pt/C + RuO_2-based ZAB (1.43 V, 122.1 mW cm^{-2}), demonstrating its superior discharge performance. Furthermore, at a constant current density of 5 mA cm^{-2}, the specific capacity of the Zr_3/NG-based ZAB reaches 744.8 mA h g_{Zn}^{-1} (Fig. 5d), exceeding that of the Pt/C + RuO_2-based ZAB (722.4 mA h g_{Zn}^{-1}). Fig. 5e presents the stabilized discharge plateaus of Zr_3/NG and Pt/C + RuO_2 at various current densities. It can be seen that the output voltage of the Zr_3/NG-based ZAB at

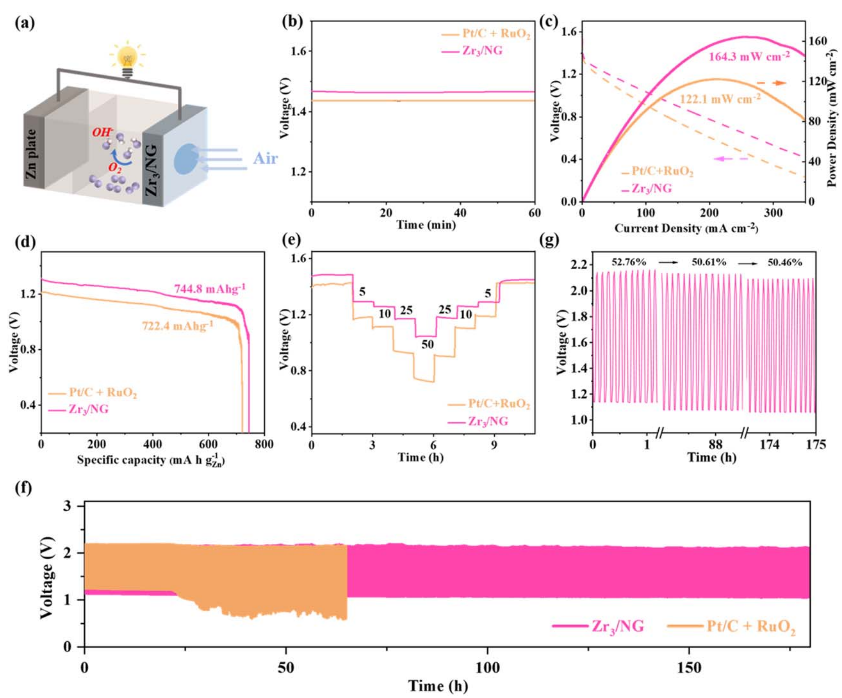

Fig. 5 (a) Schematic diagram of the self-assembled ZAB. (b) Comparison of open-circuit voltage between the Zr_3/NG-based ZAB and Pt/C + RuO_2-based ZAB. (c) Comparison of polarization curves. (d) The specific capacity. (e) Step plots. (f) The cycle stability. (g) The efficiency diagram.

each step is significantly higher than that of Pt/C + RuO_2, reflecting its better constant-current discharge capability. Charge–discharge cycling stability is a critical indicator for evaluating ZAB performance. Remarkably, after over 1000 cycles (≈175 h), the Zr_3/NG cathode exhibits highly stable cycling, demonstrating excellent long-term stability (Fig. 5f). In contrast, the Pt/C + RuO_2 based battery begins to degrade after about 60 h of stable operation and eventually deactivates. In addition, we conducted an extended continuous cycling test for up to 500 hours to evaluate the anti-dissolution properties of zirconium metal. The results show that the battery exhibited excellent stability, confirming the outstanding anti-dissolution properties of Zr metal (Fig. S17). Notably, the round-trip efficiency of the Zr_3/NG-based ZAB initially reaches 52.76% and decreases by only 2.3% after 175 h of continuous cycling (Fig. 5g), further confirming the outstanding and stable electrocatalytic activity of Zr_3/NG in the assembled ZAB.

Conclusions

In summary, this study successfully constructed a zirconium-based triatomic catalyst Zr_3/NG with $Zr_3O_1N_6$ active sites on nitrogen-doped graphene *via* a Joule-heating method, which demonstrates excellent ORR activity under alkaline conditions. The synthesis method enables instantaneous high temperature and rapid cooling, which facilitate the formation of atomically dispersed active sites. DFT calculations revealed that the synergistic effect and electronic rearrangement of the $Zr_3O_1N_6$ active sites are vital to efficient ORR catalysis. The modulation of the d-band center and the density of states in Zr_3/NG promote the adsorption and desorption of oxygen-containing intermediates, thereby accelerating the reaction kinetics. The $Zr_3O_1N_6$ structure constructed in this work is expected to optimize the ORR pathway through the synergistic interaction of the trinuclear zirconium clusters and the electronic regulation of the bridging oxygen atom. Therefore, this study proposes a new strategy for engineering efficient ORR electrocatalysts with triatomic active sites and studying the catalytic mechanisms.

Author contributions

Anaer Husile: investigation, data curation, writing – original draft; Tianmi Tang: investigation; Liyuan Xiao: investigation; Xue Bai: investigation; Zhenlu Wang: investigation; Jingqi Guan: conceptualization, methodology, writing – review and editing, supervision.

Conflicts of interest

There are no conflicts to declare.

Data availability

The data supporting this article have been included as part of the supplementary information (SI). Supplementary information is available. See DOI: https://doi.org/10.1039/d6sc01335j.

Acknowledgements

This work was supported by the National Natural Science Foundation of China (No. 92580106 and No. 22075099), the Natural Science Foundation of Jilin Province (No. 20260102152JC), and the Graduate Innovation Fund of Jilin University (No. 2025CX114). The authors acknowledge the BL11B beamline (31124.02.SSRF.BL11B) of the Shanghai Synchrotron Radiation Facility (SSRF) for providing the XAFS beamtime.

Notes and references

1 S. Guo, Y. Du, H. Luo, Z. Zhu, T. Ouyang and Z. Liu, Stabilizing Undercoordinated Zn Active Sites through Confinement in CeO_2 Nanotubes for Efficient Electrochemical CO_2 Reduction, *Angew. Chem., Int. Ed.*, 2023, **63**, e202314099.
2 X. Liu, T. Liu, T. Ouyang, J. Deng and Z. Q. Liu, Ce^{3+}/Ce^{4+} Ion Redox Shuttle Stabilized $Cu^{\delta+}$ for Efficient CO_2 Electroreduction to C_2H_4, *Angew. Chem., Int. Ed.*, 2024, **64**, e202419796.
3 (*a*) Q. Yan, X. Lin, J. Liu, T. Ouyang and Z. Liu, Engineering the electronic structure of Ni-Co bimetallic sites toward efficient electrochemical biomass upgrading and CO_2 reduction, *Chem. Sci.*, 2026, **17**, 5430–5441; (*b*) X. Xu and J. Guan, Spin effect in dual-atom catalysts for electrocatalysis, *Chem. Sci.*, 2024, **15**, 14585–14607.
4 L. Li, X. Tang, B. Wu, B. Huang, K. Yuan and Y. Chen, Advanced Architectures of Air Electrodes in Zinc-Air Batteries and Hydrogen Fuel Cells, *Adv. Mater.*, 2023, **36**, 2308326.
5 R. Huang, M. Y. Wang, J. Xiong, H. Zhang, J. Tain and J. Li, Anode optimization strategies for zinc-air batteries, *eScience*, 2025, **5**, 100309.
6 Z. Cui, G. Fu, Y. Li and J. B. Goodenough, Ni_3FeN-Supported Fe3Pt Intermetallic Nanoalloy as a High-Performance Bifunctional Catalyst for Metal-Air Battery, *Angew. Chem., Int. Ed.*, 2017, **56**, 9901–9905.
7 J. N. Liu, B. Q. Li, C. Zhao, J. Yu and Q. Zhang, A Composite Bifunctional Oxygen Electrocatalyst for High-Performance Rechargeable Zinc-Air Batteries, *ChemSusChem*, 2020, **13**, 1529–1536.
8 C. Lim, A. R. Fairhurst, B. J. Ransom, D. Haering and V. R. Stamenkovic, Role of transition metals in Pt alloy catalysts for the oxygen reduction reaction, *ACS Catal.*, 2023, **13**, 14874–14893.
9 Q. Ren, H. Wang, X. Lu, Y. X. Tong and G.-R. Li, Recent progress on MOF-derived heteroatom-doped carbon-based electrocatalysts for oxygen reduction reaction, *Adv. Sci.*, 2017, **5**, 1700515.
10 P. Zhang, J. S. Wei, X. B. Chen and H. M. Xiong, Heteroatom-doped carbon dots based catalysts for oxygen reduction reactions, *J. Colloid Interface Sci.*, 2019, **537**, 716–724.
11 X. Wang, Y. An, L. Liu, L. Fang, Y. Liu, J. Zhang, H. Qi, T. Heine, T. Li, A. Kuc, M. Yu and X. Feng, Atomically dispersed pentacoordinated-zirconium catalyst with axial

oxygen ligand for oxygen reduction reaction, *Angew. Chem., Int. Ed.*, 2022, **61**, e202209746.

12 X. Zhang, P. Lu, X. Cui, L. Cui, C. Zhang, M. Li, Y. Xu and J. Shi, Probing the electro-catalytic ORR activity of cobalt-incorporated nitrogen-doped CNTs, *J. Catal.*, 2016, **344**, 455–464.

13 G. M. Pereira, T. S. P. Cellet, M. E. G. Winkler, A. F. Rubira and R. Silva, Printing specific active sites for ORR and hydrazine oxidation on N-doped carbon, *Mater. Chem. Phys.*, 2023, **307**, 1288102.

14 H. Jeong, S. Shin and H. Lee, Heterogeneous atomic catalysts overcoming the limitations of single-atom catalysts, *ACS Nano*, 2020, **14**, 14355–14374.

15 D. Deng, J. Qian, X. Liu, H. Li, D. Su, H. Li, H. Li and L. Xu, Non-covalent interaction of atomically dispersed Cu and Zn pair sites for efficient oxygen reduction reaction, *Adv. Funct. Mater.*, 2022, **32**, 2203471.

16 Y. Liu, Y. Yang, X. Lin, Y. Lin, Z. Zhuo, D. Liu, J. Mao and J. Jiang, The geometric-electronic coupled design of diatomic catalyst towards oxygen reduction reaction, *Nat. Commun.*, 2025, **16**, 5158.

17 W. Gong, H. Arman, Z. Chen, Y. Xie, F. A. Son, H. Cui, X. Chen, Y. Shi, Y. Liu, B. Chen, O. K. Farha and Y. Cui, Highly specific coordination-driven self-assembly of 2D heterometallic metal-organic frameworks with unprecedented johnson-type(J_{51}) nonanuclear Zr-oxocarboxylate clusters, *J. Am. Chem. Soc.*, 2021, **143**, 657–663.

18 B. Chi, L. Zhang, X. Yang, Y. Zeng, Y. Deng, M. Liu, J. Huo, C. Li, X. Zhang, X. Shi, Y. Shao, L. Gu, L. Zheng, Z. Cui, S. Liao and G. Wu, Promoting ZIF-8-derived Fe-N-C oxygen reduction catalysts via Zr doping in proton exchange membrane fuel cells: durability and activity enhancements, *ACS Catal.*, 2023, **13**, 4221–4230.

19 Y. Lu, X. Xie and W. Fang, Insight into the property modification of Zr-incorporated alumina binary mixed oxides by XRD, TEM, XPS, TPD and IR, *ChemistrySelect*, 2020, **5**, 7928–7933.

20 S. Zhang, X. Bai, T. Tang, W. Ruan and J. Guan, Coordination modulation of single-atom Zn sites to boost oxygen reduction performance, *Inorg. Chem. Front.*, 2025, **12**, 2917–2924.

21 J. Sun, Z. Wang and J. Guan, Single-atom Ce catalysts for rechargeable Zn-air batteries, *Mater. Chem. Front.*, 2025, **9**, 1574–1580.

22 X. Xu, T. Tang, G. Zhang and J. Guan, Tuning electronic structure of cobaltous nitride-manganous oxide heterojunction by N-vacancy engineering for optimizing oxygen electrocatalysis activity, *Nano Energy*, 2024, **131**, 110294.

23 J. Xu, Y. Zhao, C. Shen and L. Guan, Sulfur-and nitrogen-doped, ferrocene-derived mesoporous carbons with efficient electrochemical reduction of oxygen, *ACS Appl. Mater. Interfaces*, 2013, **5**, 12594–12601.

24 G. Yang, M. Fan, Q. Liang, X. He, W. Zhang and T. Asefa, Atomically Dispersed Fe2 and Ni Sites for Efficient and Durable Oxygen Electrocatalysis, *Angew. Chem., Int. Ed.*, 2024, **64**, e202421168.

25 H. Jung, S. M. Paek, J.-B. Yoon and J. H. Choy, Zr K-edge XAS study on ZrO_2-pillared aluminosilicate, *J. Porous Mater.*, 2007, **14**, 369–377.

26 P. A. Kots, A. V. Zabilska, E. V. Khramov, Y. V. Grigoriev, Y. V. Zubavichus and I. I. Ivanova, Mechanism of Zr incorporation in the course of hydrothermal synthesis of zeolite BEA, *Inorg. Chem.*, 2018, **57**, 11978–11985.

27 Y. Li, Y. Ding, B. Zhang, Y. Huang, H. Qi, P. Das, L. Zhang, X. Wang, Z.-S. Wu and X. Bao, N,O symmetric double coordination of an unsaturated Fe single-atom confined within a graphene framework for extraordinarily boosting oxygen reduction in Zn-air batteries, *Energy Environ. Sci.*, 2023, **16**, 2629–2636.

28 Y. Zhang, W. Xue, Y. Ding, H. Chen and X. Xu, FeCo alloy modified MoN electrocatalyst with excellent ORR and OER activities for Zn-air battery, *Inorg. Chem. Commun.*, 2025, **177**, 114374.

29 S. Ravinder, S. Arkaj and H. Aditi, Synergistic effect of lattice strain, oxygen vacancy and morphology in Mo doped $NiCo_2O_4$ for high-performance zinc air batteries, *J. Energy Storage*, 2024, **107**, 114918.

30 J. Nie, M. Dong, G. Chen, N. Wang, J. Nie and G. Ma, Biomass-based hierarchical porous ORR and OER bifunctional catalysts with strong stability for Zn-air batteries, *ACS Sustain. Chem. Eng.*, 2023, **11**, 11161–11171.

31 L. Qi, X. Bai, Y. Wang, Z. Duan, L. Li and J. Guan, Potential-driven structural evolution of single-atom rhenium sites enables high-performance oxygen electrode reaction and rechargeable Zn-air battery, *CCS Chem.*, 2024, **7**, 2508–2519.

32 L. Qi, Y. Tang, T. Gan and J. Guan, Engineering O-O formation on dual-atom Fe-Mo catalysts for oxygen electrocatalysis, *Chem. Sci.*, 2025, **17**, 516–525.

33 X. Xu, T. Tang, X. Bai, T. Gan and J. Guan, Engineering d–p orbital hybridization of single-atom Fe sites via axial B-mediation for the oxygen reduction reaction, *Chem. Sci.*, 2025, **17**, 1105–1115.